New Semi-Analytical Insights into Stress-Dependent Spontaneous Imbibition and Oil Recovery in Naturally Fractured Carbonate Reservoirs

A. H. Haghi[1], R. Chalaturnyk[1], S. Geiger[2]

[1] Reservoir Geomechanics Research Group, University of Alberta, Edmonton, Canada.

[2] Institute of Petroleum Engineering, Heriot-Watt University, Edinburgh, UK.

Corresponding author: Amir H. Haghi (haghi@ualberta.ca)

Key Points:

- Effective stress changes within the pore spaces will cause changes in the dimensions of pore spaces
- Change in pore size leads to changes in capillary diffusion
- Stress-dependent capillary diffusion directly affects imbibition and oil recovery in naturally fractured carbonate reservoirs

This article has been accepted for publication and undergone full peer review but has not been through the copyediting, typesetting, pagination and proofreading process which may lead to differences between this version and the Version of Record. Please cite this article as doi: 10.1029/2018WR024042

Abstract

Fluid injection and withdrawal in a porous medium create changes in pore pressure that alter effective stresses within the medium. This leads to pore volume changes, which can be described by the poroelastic theory. These changes in pore volume can influence fluid flow processes, such as capillary diffusion and imbibition, potentially altering multiphase flow characteristics in subsurface reservoirs with a focus on oil recovery in the naturally fractured carbonate reservoirs (NFCRs). In this study, a semi-analytical model is developed to analyze the impact of stress-dependent spontaneous imbibition. The model allows us to study the influence of stress-dependent effects on porosity, absolute permeability, relative permeability, and capillary pressure on the imbibition and oil recovery mechanisms of both intact rock and fracture in NFCRs. In order to capture the geomechanical interactions involved, pure compliance poroelastic definitions and nonlinear joint normal stiffness equations are used to assess the deformation of intact rock and fracture, respectively. The model shows that increasing effective confining stress shifts the imbibition capillary pressure curve upward, resulting in improved absorption of the wetting phase into the smaller pores and enhanced extraction of the non-wetting phase. Model calculations provide a rationale for how and why irreducible water saturation increases during compression of mixed-wet carbonates and decreases in the case of initially strong water-wet carbonates. It is also shown how higher relative permeability of the wetting phase leads to a greater diffusion of the wetting phase and improved oil recovery for the less deformed mixed-wet rock.

1 Introduction

The objective of this study is to develop relationships for stress dependent static/dynamic flow properties and analyze how they influence spontaneous imbibition and oil recovery. Counter-current spontaneous imbibition is the dominant production mechanism in fractured reservoirs in cases in which matrix blocks are not fully surrounded by water [*Pooladi-Darvish and Firoozabadi*, 2000]. For this application, a new definition of capillary-driven fractional flow is presented taking into account the effect of porosity changes over time. Dynamic porosity, dynamic permeability, and geo-dynamic rock properties are then specified for a dual continuum model (e.g. carbonate matrix and fracture). We have chosen the term *geo-dynamic* to refer to initially dynamic properties such as relative permeability and capillary pressure that vary due to *geo*mechanical processes.

Natural fractures are a common feature in nearly all hydrocarbon reservoirs that can significantly influence oil recovery and reservoir performance [*Ahmed and McKinney*, 2011]. This study focuses on naturally fractured carbonate reservoirs (NFCRs) classified as Type II [*Nelson*, 2001], in which fractures provide most of the reservoir's permeability, while the rock matrix provides its main hydrocarbon storage capacity.

For this class of reservoirs, the success of recovery techniques such as water flooding or alkaline surfactant polymer flooding (ASP) is negatively impacted by the limited pressure difference that arises in the reservoir as a result of highly permeable fractures dominating fluid flow. In these cases, capillary imbibition, as opposed to viscous displacement, becomes the dominant recovery mechanism enabling hydrocarbon to flow from the matrix into the fracture system. Counter-current spontaneous imbibition is an essential recovery mechanism in NFCRs, and its performance is determined by the capillary pressure curve, which is a function of pore structure and wettability [*Ferno*, 2012]. Increasingly, there has been a recognition that the geomechanical behavior of NFCRs can influence hydrocarbon recovery [*Settari et al.*, 1999].

Surprisingly little has been published regarding the stress-dependent relative permeability of the matrix or intact rock within NFCRs. *Li and Horn* [2006] presented the commonly used modified Brooks and Corey relation [*Corey*, 1954; *Brooks and Corey*, 1966] to describe capillary pressure (P_c) and relative permeability of the wetting (k_{rw}) and non-wetting (k_{rnw}) phases:

$$P_c = P_e (S_w^*)^{\beta} \tag{1}$$

$$k_{rw} = k_{rw-max} (S_w^*)^{n_w} \tag{2}$$

$$k_{rnw} = k_{rnw-max} (1 - S_w^*)^{n_{nw}} \tag{3}$$

$$S_w^* = \frac{S_w - S_{wir}}{1 - S_{wir} - S_{nwr}} \tag{4}$$

where S_{wir} and S_{nwr} refer to the irreducible wetting and residual non-wetting phase saturation. Additionally, P_e, k_{rw-max}, and $k_{rnw-max}$ denote entry capillary pressure (threshold pressure), and the maximum relative permeability of the wetting and non-wetting phases, respectively.

The power law coefficients β, n_w, and n_{nw} can be related to the pore size distribution index λ^* ($\lambda^* > 0$) [*Brooks and Corey*, 1966], with the following equations:

$$\beta = -\frac{1}{\lambda^*} \tag{5}$$

$$n_w = \frac{A + B\lambda^*}{\lambda^*} \tag{6}$$

$$n_w = \frac{A' + B'\lambda^*}{\lambda^*} \tag{7}$$

where A, A', B, and B' are curve-fitting constants. These can be estimated using the least square method on the experimental data.

The bundle of capillary tubes illustrated in Figure 1 serves as an analogue to pore size distribution and the index λ^*. For a given, original pore size distribution, the black curve shown in Figure 1 illustrates the process of spontaneous imbibition, as the wetting phase saturation increases with decreasing capillary pressure over a range of pore sizes (i.e. capillary tube diameter). For cases in which increasing effective stress leads to a reduction in pore sizes (i.e. a reduction in capillary tube diameters), the change in the red curve in Figure 1 illustrates how the capillary curve shifts upwards, altering the spontaneous imbibition characteristics of the matrix. In the case illustrated in Figure 1, effective stress induced-deformation enhances the imbibition process. Alternatively, if effective stress changes lead to increases in pore sizes, the spontaneous imbibition process is attenuated. Given the importance of quantifying the imbibition process under these conditions, understanding and quantifying the stress-dependent dynamic properties in NFCRs is critical for improving field recovery and optimizing reservoir management.

2 Experimental Results

In terms of laboratory experiments, there is little data showing effective stress effects on relative permeability in NFCRs. For this study, the results from experiments conducted by *McDonald et al.* [1991] and *Lian et al.* [2012] are analyzed to establish the key parameters required for the semi-analytical model. Both experimental programs demonstrated the stress dependency of oil-water relative permeability in fractured carbonates. The experimental results from *Lian et al.* [2012], shown in Figure 2, indicate that the irreducible wetting phase (water) saturation, S_{wir}, increases with effective confining stress, σ', while the water relative permeability,
k_{rw}, shifts to the right. This behavior suggests the rock becomes increasingly water-wet as effective stress increases. In contrast, the experimental results from *McDonald et al.* [1991], shown in Figure 3, indicate that increasing stress results in a reduction of irreducible water saturation and causes the relative permeability curves to shift to the left.

Hue and Benson [2016] concluded that this apparent contradiction in behavior can be explained by the relative weight of viscous and capillary forces, termed the *capillary number*. The capillary number is defined as [*Peters*, 2012]:

$$N_c = \frac{\mu V}{\sigma_{st} \cos\theta} \tag{8}$$

where μ is the dynamic viscosity of the liquid, V is a characteristic velocity and $\sigma_{st} \cos\theta$ is the surface or interfacial tension between the two fluid phases. The authors concluded that under constant capillary number conditions, the irreducible water saturation increases with increasing effective confining stress (as in the case of *Lian et al.*, [2012]). However, in experiments with a constant flow rate, higher effective confining stress decreases the irreducible water saturation (case of [*McDonald et al.*, 1991]).

The relative permeability curves from *Lian et al.* [2012], Figure 2, and *McDonald et al.* [1991], Figure 3, are based on lab experiments on mainly mixed-wet and strongly water-

wet carbonates, respectively. Otherwise, the wetting phases differ between the tests. Accordingly, the results from the two experimental programs are consistent and show an increase in the irreducible saturation of the wetting phase as the confining stress and capillary pressure increase. Consequently, the results from both experimental programs are utilized in this study.

Implementing the least square technique, equations (2) to (4) have been utilized to find the best match for the stress-dependent relative permeability data from both *McDonald et al.* [1991] and *Lian et al.* [2012]. Figure 2 illustrates the relative permeability curve correlation for 10 MPa and 30 MPa effective confining stress based on modified Brooks-Corey relations combined with data presented by *Lian et al.* [2012].

Table 1 provides the equations for the given fitting curves illustrated in Figure 2. Similarly, Figure 3 shows the relative permeability curve for 6.9 MPa (0.36 mm fracture aperture) and 26.5 MPa (0.15 mm fracture aperture) effective confining stress based on the modified Brooks-Corey relations (see Table 2) and data presented by *McDonald et al.* [1991].

3 Derivation of Semi-Analytical Model

In this section, a semi-analytical solution is derived to model the stress-dependent spontaneous imbibition in a cubic block of rock. Analogues with *Warren and Root's* [1963] sugar cube model, orthogonal fracture sets inside the block are assumed to be perpendicular to the plane surface of the cubic matrix block (Figure 4), and three principal stresses are applied normal to the sides of the block. Section 3.1 describes the solution of the capillary diffusivity equation considering a time- (or effective stress-) dependent porosity for the counter-current imbibition of the wetting phase on each side of the block. Sections 3.2.1 and 3.3.1 describe the stress-dependent porosity of the block using poroelastic theory and nonlinear joint normal stiffness equations for intact rock and fracture deformations, respectively. Sections 3.2 to 3.4 provide the solutions for absolute permeability, relative permeability, and capillary pressure, which are updated in each effective stress condition, using appropriate theories for the dual medium. We have assumed that the matrix-fracture's effects can be added as an averaged two-medium property to the block model in Figure 4 and that the medium properties are distributed uniformly.

3.1 Stress Dependent Counter-Current Fractional Flow Formulation

Rewriting the mass-balance equation for two phase flow in 1D (each side of the block) for incompressible phase ($\rho_w = cte$) at constant temperature through homogeneous porous media with porosity (φ), we obtain the continuity equation [*Bears*, 2013]

$$\frac{\partial}{\partial t}(S_w \varphi) = -\frac{\partial q_w}{\partial x}. \tag{10}$$

We assume that the flow rate of the wetting and non-wetting phase, q_w and q_{nw}, respectively, can be specified by the Darcy equation [*Peters*, 2012]

$$q_w = -\frac{k k_{rw}}{\mu_w}\left(\frac{\partial P_w}{\partial x} + \rho_w g sin\alpha\right) \text{ and} \tag{11}$$

$$q_{nw} = -\frac{k k_{rnw}}{\mu_{nw}}\left(\frac{\partial P_{nw}}{\partial x} + \rho_{nw} g sin\alpha\right), \tag{12}$$

where k is the absolute permeability, μ_w is the viscosity of the wetting phase, μ_{nw} is the viscosity of the non-wetting phase, and k_{rnw} and k_{rw} are the relative permeability of the non-wetting phase and the wetting phase, respectively. Combining equations (11) and (12) results in the following equation:

$$\frac{q_w\mu_w}{kk_{rw}} - \frac{q_{nw}\mu_{nw}}{kk_{rnw}} = \frac{\partial P_{nw}}{\partial x} - \frac{\partial P_w}{\partial x} - \Delta\rho g sin\alpha \ . \tag{13}$$

Using the definitions for capillary pressure (P_c), fractional flow (f), total flow (q_t), and the mobility ratio (λ), equation (13) can be rewritten as [*Peters*, 2012]:

$$q_w = \frac{\lambda_w}{\lambda_t} q_t + k\frac{\lambda_w\lambda_{nw}}{\lambda_t}\frac{\partial P_c}{\partial x} - k\frac{\lambda_w\lambda_{nw}}{\lambda_t}\Delta\rho g sin\alpha \ . \tag{14}$$

Equation (14) shows that water velocity is a result of the total viscous velocity, a gradient in capillary pressure and gravity, as represented by the first, second and third terms on the right hand side of equation, respectively. Ignoring capillary and gravity forces (by setting the second and third terms in equation (14) to zero), the Buckley-Leverett solution can be derived [*Ahmed and McKinney*, 2011]. Considering counter-current spontaneous imbibition ($q_t = 0$) but ignoring the gravitational forces (third terms), equation (14) becomes

$$q_w = -D\frac{\partial S_w}{\partial x} \ . \tag{15}$$

Herein, we used the chain rule for the capillary gradient ($\frac{\partial P_c}{\partial x} = \frac{\partial P_c}{\partial S_w} \times \frac{\partial S_w}{\partial x}$) and the nonlinear capillary diffusion coefficient with the unit of length squared over time (equation 16) [*McWhorter and Sunada*, 1990]. In this study we considered D to be not only a function of wetting phase saturation, but also, since the rock properties are stress-dependent, a function of effective stress in the reservoir:

$$D(S_w, \sigma') = -\frac{k\lambda_w\lambda_{nw}}{\lambda_t}\frac{\partial P_c}{\partial S_w} \ . \tag{16}$$

Replacing q_w in equation (10) with the derived q_w in equation (15) leads to equation (17) for capillary imbibition. As rock porosity is effective stress-dependent, and effective stress changes with time, in this study we consider it to be a dynamic rock property. Accordingly, the general partial differential equation for counter-current spontaneous imbibition flow with deforming rock assumption is specified as follows:

$$S_w\frac{\partial\varphi}{\partial t} + \varphi\frac{\partial S_w}{\partial t} = \frac{\partial}{\partial x}\left(D(S_w, \sigma')\frac{\partial S_w}{\partial x}\right) \ . \tag{17}$$

Note that $D(S_w, \sigma')$ is zero if $S_w = S_{wir}$. Table 3 provides the initial and boundary conditions for equation (17). *Schmid et al.* [2016] used the similarity variable $\omega = x/\sqrt{t}$ and presented a general solution in terms of the derivative of a capillary-driven fractional flow function (F) as follows:

$$\omega(S_w) = \frac{2C}{\varphi}\frac{\partial F}{\partial S_w} \ , \tag{18}$$

where C is deemed to be proportionality constant with the unit of m/√s (C^2 has the units of a diffusion coefficient) and is specified as follows:

$$q_w(x = 0, t) = \frac{C}{\sqrt{t}} \ . \tag{19}$$

In this study, the parameter ω is used to describe capillary-driven spontaneous imbibition.

Appendix A provides a proof that the similarity variable ω, given in equation (18), is valid for the class of problem presented in this research. The proportionality constant, C, controls the imbibition of the wetting phase at the inlet (x=0) of rock, and it is a function of flow parameters such as relative permeability, capillary pressure, and viscosity. In this study, C is not a constant but an effective stress dependent parameter (C') since static and dynamic flow properties change with rock deformation.

Similarly, ω is also a stress-dependent variable. Given the similarity between the capillary-driven flow equation (18) and the Buckley-Leverett viscous-driven flow equation [*Peters*, 2012], *Schmid and Geiger* [2012] concluded that F is the fractional flow function for the case of capillary-driven flow. Hence, F is given by the ratio of water flow as a function of saturation to its maximum value at the inlet. Equation (17) now becomes

$$S_w \omega \frac{d\varphi}{d\omega} + \varphi\omega \frac{dS_w}{d\omega} = -2\frac{d}{d\omega}\left(D(S_w, \sigma')\frac{dS_w}{d\omega}\right), \tag{20}$$

using the following relations:

$$\frac{\partial S_w}{\partial t} = \frac{\partial S_w}{\partial \omega}\frac{\partial \omega}{\partial t} = -\frac{\omega}{2t}\frac{dS_w}{d\omega} \tag{21}$$

$$\frac{\partial S_w}{\partial x} = \frac{\partial S_w}{\partial \omega}\frac{\partial \omega}{\partial x} = \frac{1}{\sqrt{t}}\frac{dS_w}{d\omega} \tag{22}$$

$$\frac{\partial \varphi}{\partial t} = \frac{\partial \varphi}{\partial \omega}\frac{\partial \omega}{\partial t} = -\frac{\omega}{2t}\frac{\partial \varphi}{\partial \omega}. \tag{23}$$

Integrating both sides of equation (20) leads to the following equation,

$$\int_{\varphi_i}^{\varphi_t} S_w \omega d\varphi + \int_{S_{wir}}^{1-S_{or}} \varphi\omega dS_w = -2D(S_w, \sigma')\frac{dS_w}{d\omega}, \tag{24}$$

where φ_t is the dynamic porosity. The term *dynamic* is used to emphasize the fact that porosity is not a static rock property in the model, but a dynamic property that changes with stress based on poroelastic theory. Meanwhile, φ_t is uniform in space. Note that the integral limits in equation (24) for the similarity variable ω are zero to $(L/2)/\sqrt{t^*}$ (or $x = 0$ to $L/2$) for the finite block of rock with a dimension of L (Figure 4). Here, the early time imbibition, t^*, is defined as follows:

$$t^* = \left(\frac{L}{2\omega(S_{wir})}\right)^2. \tag{25}$$

Assuming S_w and φ are independent parameters, and replacing ω with the terms given in equation (18), equation (24) can be written as follows:

$$\left(S_w \, ln(\varphi_t/\varphi_i)\frac{dF}{dS_w} + F\right)\frac{d^2F}{dS_w{}^2} = -\frac{\varphi_t}{2C'^2}\, D(S_w, \sigma'). \tag{26}$$

Equation (26) can be solved both analytically and numerically using the finite difference approximation method. Herein, we propose a numerically backward-differencing approximation to solve equation (26).

$$F_1 = -BF_2 - 0.5F_3 + \sqrt{B^2F_2^2 + 0.25F_3^2 + BF_2F_3 - \frac{1}{(1-A)}(AF_2F_3 - 2AF_2^2 + \frac{\varphi_t}{2C'^2}\, D(S_w, \sigma')\Delta S_w{}^2}, \tag{27}$$

where $A = \frac{S_w \ln(\varphi_t/\varphi_i)}{\Delta S_w}$ and $B = \frac{(3A-2)}{2(1-A)}$ are simplifying parameters. Classical approaches, which neglect porosity change ($\varphi_t = \varphi_i$), employ $A = 0$ and $B = -1$; this reduces equation (27) to the definition of capillary-driven fractional flow term presented by *Schmid et al.* [2016]. In equation (27), F_1, F_2, and F_3 refer to $F(S_w)$, $F(S_w + \Delta S_w)$, and $F(S_w + 2\Delta S_w)$,

respectively. From equation (27), we can determine F at each saturation, which allows $\frac{\partial F}{\partial S_w}$ to be inserted into equation (18) to obtain the saturation distribution with ω. However, equation (27) still requires that we know C' and the stress dependent rock properties at each stress condition (e.g. φ_t, $D(S_w, \sigma')$). The parameter C' can be computed by choosing a starting value and iterating it until some convergence criteria for F (e.g. $F(S_w = S_{wir}) = 0$ and $F(S_w = 1) = 0$) at each effective stress state is met [*Schmid et al.* 2016]. To specify the stress-dependent rock properties for such a dual continuum model, we need to determine the property for each media separately and mix them together to find the equilibrium continuum properties [*Bagheri and Settari*, 2008]. Hence, to define φ_t and $D(S_w, \sigma')$ in equation 27, we need to derive representative equations for stress-dependent porosity, absolute permeability, relative permeability, and capillary pressure for a block of rock which contains both fracture and intact rock. In the following sections (3.2 to 3.4), additional expressions are developed for these stress-dependent rock properties.

3.2 Matrix Stress-Dependent Properties Specification

3.2.1 Matrix Dynamic Porosity (φ_{mt})

The effective constitutive relation (stress-strain) for intact rock is assumed to follow Hooks's law and mathematically takes the following form in index notation [*Bagheri and Settari*, 2008]:

$$\varepsilon_{ij} = C_{ijkl}\sigma'_{kl} \tag{28}$$

where ε_{ij} is the strain tensor, σ'_{kl} is the effective stress tensor for porous media, and C_{ijkl} is a 6×6 stiffness matrix. The constitutive equation in which strain and increment of fluid content are paired as dependent variables, and stress and pore pressure are considered independent variables, is called the pure compliance model [*Wang*, 2017]. The poroelastic constitutive equation for the pure compliance model is given as follows [*Segal*, 1989]:

$$\varepsilon_{ij} = \frac{1}{2G}\left(\sigma_{ij} - \left(\frac{\vartheta}{1+\vartheta}\right)\sigma_{kk}\delta_{ij} + \left(\frac{1-2\vartheta}{1+\vartheta}\right)\alpha P\delta_{ij}\right) \tag{29}$$

where ϑ, α and G are drained Poisson's ratio, Biot coefficient, and shear modulus, respectively. The strain and stress tensors each contain six components for an arbitrary orientation of the coordinates system. However, for deep oil and gas reservoirs, it is common to use principal coordinates in which shear stress and shear strains are zero. This is the case here, as we assumed the principal effective stresses were perpendicular to the plane surface of the cubic matrix block (Figure 5). The three principal strains corresponding to three principal stresses based on equation (29) are specified as follows:

$$\varepsilon_x = \frac{1}{2G}\left(\sigma_x - \left(\frac{\vartheta}{1+\vartheta}\right)(\sigma_y + \sigma_z) + \left(\frac{1-2\vartheta}{1+\vartheta}\right)\alpha P\right) \tag{30}$$

$$\varepsilon_y = \frac{1}{2G}\left(\sigma_y - \left(\frac{\vartheta}{1+\vartheta}\right)(\sigma_x + \sigma_z) + \left(\frac{1-2\vartheta}{1+\vartheta}\right)\alpha P\right) \tag{31}$$

$$\varepsilon_z = \frac{1}{2G}\left(\sigma_z - \left(\frac{\vartheta}{1+\vartheta}\right)(\sigma_x + \sigma_y) + \left(\frac{1-2\vartheta}{1+\vartheta}\right)\alpha P\right). \tag{32}$$

Accordingly, the volumetric strain can be computed as (*Wang*, 2000)

$$\varepsilon_v(t) = \varepsilon_x + \varepsilon_y + \varepsilon_z = \frac{(1-\vartheta)}{E}(\sigma_x(t) + \sigma_y(t) + \sigma_z(t)) + \frac{\alpha}{K}P(t) \tag{33}$$

where $E = 2G(1+\vartheta)$ is drained Young's modulus, and $K = \frac{E}{3(1-2\vartheta)}$ is bulk modulus. Assuming equal horizontal stress, $\sigma_x = \sigma_y = \sigma_3$, and $\sigma_z = \sigma_1$, we have

$$\varepsilon_v(t) = \varepsilon_x + \varepsilon_y + \varepsilon_z = \frac{2(1-\vartheta)}{E}\sigma_3(t) + \frac{(1-\vartheta)}{E}\sigma_1(t) + \frac{\alpha}{k}P(t). \quad (34)$$

In equation (34), the signs of σ_i and ε_i for compression are negative. Knowing the volumetric strain, the dynamic porosity of the intact rock can be computed as follows [*Tortike and Ali*, 1993*; Li and Chalaturnyk*, 2003]:

$$\varphi_{mt} = \frac{V_{pi} + \Delta V_p}{V_{bi} + \Delta V_b} = \frac{V_{pi} + (\Delta V_b - \Delta V_s)}{V_{bi} + \Delta V_b} \times \frac{V_{bi}}{V_{bi}} = \frac{\varphi_{mi} + \varepsilon_v - {}^{\Delta V_s}/_{V_{bi}}}{1 + \varepsilon_v} = \frac{\varphi_{mi} + \varepsilon_v(t)}{1 + \varepsilon_v(t)} \quad (35)$$

where $V_\alpha, \alpha = b, p, s$ indicates bulk, pore and grain volume, respectively. Given the relative incompressibility of the grains, the term ${}^{\Delta V_s}/_{V_{bi}}$ has been neglected in the formulation. Equation (35) allows the matrix porosity component of the total porosity in the capillary diffusion solution given in equation (27) to be updated at each effective stress condition. The fracture porosity component of the total porosity is described in Section 3.3.1.

3.2.2 Matrix Dynamic Absolute Permeability (k_{mt})

For the initial stage of model development, we have adopted the widely-used Carman-Kozeny relation to express absolute permeability as a function of porosity [*Carman*, 1956]. Assuming *n* number of parallel and equal capillary tubes inside the block of matrix in Figure 5, we investigate the effect of deformation on the absolute permeability of the intact rock. Based on Hagen-Poiseuille's law for the steady, laminar flow of Newtonian fluid through a bundle of *n* number capillary tubes of radius r, the flow rate can be determined as follows [*Dake*, 1983]:

$$q = -\left(\frac{n\pi r^4}{8\mu}\right)\frac{\Delta P}{l}. \quad (36)$$

In equation (36) the tortuosity term has been disregarded. Comparing this equation with the linear Darcy flow equation through a cube of dimension l ($q = -(\frac{l^2 k}{\mu})\frac{\Delta P}{l}$, Figure 5), the absolute permeability equation in terms of porosity is

$$k = \left(\frac{n\pi r^4}{8l^2}\right) = \frac{\varphi r^2}{8}. \quad (37)$$

Application of effective confining stresses on the block of intact rock in Figure 5 will result in deformation based on the poroelastic equation presented in Section 3.2.1. Hence, the ratio between the dynamic (k_{mt}) and initial (k_{mi}) absolute permeability is defined based on the following equation:

$$\frac{k_{mt}}{k_{mi}} = \frac{\varphi_{mt}}{\varphi_{mi}}\frac{r_t^2}{r_i^2} = \frac{\varphi_{mt}}{\varphi_{mi}}\frac{n\pi r_t^2}{n\pi r_i^2}\frac{l^2}{l^2} = \left(\frac{\varphi_{mt}}{\varphi_{mi}}\right)^2. \quad (38)$$

Equation (38) allows the dynamic absolute permeability to be computed. This equation is subsequently combined with an equation derived for the absolute permeability of the fracture (Section 3.3.2) to describe average absolute permeability of the whole block.

3.3 Fracture Stress-Dependent Properties Specification

Given the nonlinear deformation of fractures in response to effective stress changes, fracture properties should be treated as dynamic properties due to changing effective stresses

during production and injection operations. The following sections describe the procedure to derive fracture dynamic porosity and absolute permeability.

3.3.1 Fracture Dynamic Porosity (φ_{ft})

Fracture deformation modes will vary under the application of normal or shear stresses. In many cases, the effect of shear stresses on fracture deformation in naturally fractured reservoirs is neglected in reservoir simulations [*Bagheri and Settari*, 2008] due to the extensive lab work required to define this behavior. In addition, major difficulties exist in upscaling lab work to full field simulation models, and the effect of shear stress is less well understood than that of normal stress. Consequently, for the current semi-analytical formulation, shear stress effects have also been disregarded. Considering the fracture aperture as a narrow layer of different material than the matrix rock, we apply Hooke's law to describe the fracture stress–strain relations. As in the case of intact rock deformation, the constitutive equation to investigate deformation in fractures would be

$$d\varepsilon_{ij} = D_{ijkl}\Delta\sigma'_{kl}n_k, \tag{39}$$

where n_k represents the components of the normal vector to the joint surface [*Bagheri and Settari*, 2008]. Considering single plane fractures perpendicular to one of the principal stresses (shear displacement being disregarded) with an aperture J_o (see Figure 6), the joint stress-strain relations become [*Pariseau*, 2011]

$$d\sigma_n = k_n dJ_n, \tag{40}$$

where k_n is the fracture normal stiffness that relates stress to the relative displacement between opposing points on the two surfaces of fracture. Here, the fracture closure is considered to be positive.

There are different models of fracture deformation [*Hudson and Harrison*, 2000; *Pariseau*, 2011; *Cundall and Lemos*, 1990] including 1) the Coulomb friction, 2) the continuously-yielding joint model, and 3) the Barton-Bandis joint model.

The Coulomb friction is a linear deformation model in which the fracture aperture closes elastically up to a limit of ΔJ_{max} under normal compressive stress (Figure 7a). As illustrated in Figure 7b, the Barton-Bandis joint model is a nonlinear fracture deformation model. *Bandis et al.* [1983] and *Barton et al.* [1985] described the impacts of surface roughness on fracture deformation by developing empirical relations between stress, fracture closure, and two parameters: the joint roughness coefficient, JRC, and joint wall compressive strength, JCS.

The Barton–Bandis fracture model includes hyperbolic loading and unloading curves (Figure 7b) in which normal stress and fracture closure, ΔJ, are related by the following equation,

$$\sigma_n = \frac{\Delta J}{(a - b\Delta J)}, \tag{41}$$

where *a* and *b* are constants. Rewriting equation (41) with effective normal stress terms, the equation describing fracture closure becomes

$$\Delta J = \frac{\sigma'_n}{(k_{ni} - \frac{\sigma'_n}{\Delta J_{max}})}, \tag{42}$$

where the initial fracture normal stiffness, k_{ni}, is equal to $1/a$ and the maximum fracture closure, ΔJ_{max}, is defined as a/b. Accordingly, the expression for normal stiffness becomes

$$k_n = k_{ni}\left[1 - \frac{\sigma'_n}{(\Delta J_{max}k_{ni} + \sigma'_n)}\right]^{-2}, \tag{43}$$

which reflects the dependency of fracture normal stiffness on effective stress [*Barton et al.* 1985].

In this study, we have utilized the Barton-Bandis nonlinear deformation model, which has been acknowledged universally in the literature on NFCRs [*Bagheri and Settari*, 2008]. Considering the fracture closure model geometry shown in Figure 6, the initial single fracture porosity will be defined as:

$$\varphi_{fi} = \frac{V_{ft}}{V_b} = \frac{J_o \times L^2}{L^3} = \frac{J_o}{L}. \tag{44}$$

The dynamic fracture porosity can now be estimated using equation (44) for fracture closure using the following equation:

$$\varphi_{ft} = \frac{V_{ft}}{V_{bt}} = \frac{(J_o + \Delta J) \times L^2}{(L + \Delta J)L^2} = \frac{(j_o + \Delta J)}{(L + \Delta J)}. \tag{45}$$

Application of the Barton-Bandis non-linear fracture closure model allows the fracture porosity in the capillary diffusion solution given in equation (27) to be updated at each effective stress condition.

3.3.2 Fracture Dynamic Absolute Permeability (K_{ft})

Adopting Hagen-Poiseuille's law for steady, laminar flow of a Newtonian fluid (but this time through a slit of aperture J_o with same width and length of L) yields the following equation [*Peters*, 2012]:

$$q = -\left(\frac{L{J_o}^3}{12\mu}\right)\frac{\Delta P}{L}. \tag{46}$$

Comparing this equation with the linear Darcy equation for flow through a fracture of the same dimension, $q = -(\frac{LJ_o k}{\mu})\frac{\Delta P}{L}$ (also see Figure 6), the fracture absolute permeability can be computed as [*Peters*, 2012]

$$k = \frac{{J_o}^2}{12}. \tag{47}$$

For effective normal confining stresses on the fracture, the fracture will close or open based on the nonlinear fracture closure equation presented in equation (42). Hence, the ratio between the dynamic and initial fracture absolute permeability (k_{ft} and k_{fi}, respectively) is defined based on the following equation:

$$k_{ft} = \frac{(J_o + \Delta J)^2}{{J_o}^2} k_{fi} \tag{48}$$

3.4 Dual Continuum Stress Dependent Properties Specification

3.4.1 Total Dynamic Porosity (φ_t)

For our semi-analytical model, the dual continuum dynamic porosity is computed as follows:

$$\varphi_t = \frac{V_{ft}+V_{pt}}{V_{bt}} = \varphi_{ft} + \frac{V_{pt}}{V_{bt}} = \varphi_{ft} + \varphi_{mt}\frac{V_{bmt}}{V_{bt}}, \tag{49}$$

where V_{bmt} is the dynamic matrix bulk volume. Then,

$$\varphi_t = \varphi_{ft} + \varphi_{mt}\frac{V_{bt}-V_{ft}}{V_{bt}}. \tag{50}$$

Total dynamic porosity can be estimated as follows:

$$\varphi_t = \varphi_{ft} + \varphi_{mt}(1 - \varphi_{ft}). \tag{51}$$

In equation (51), φ_{mt} and φ_{ft} indicate the matrix and fracture dynamic porosity, which are defined by equations (35) and (45), respectively. Equation (51) specifies the dynamic porosity of the whole block of rock (φ_t), and it is inserted as a measure of stress-dependent porosity into the solution of the capillary imbibition in equation (27).

3.4.2 Total Dynamic Absolute Permeability (k_t)

Given $X \times Y \times Z$ number of plane fractures oriented parallel with $yz \times xz \times xy$ planes, respectively, for the cube shown in Figure 4, the block contains $(X-1) \times (Y-1) \times (Z-1)$ matrix blocks. The total dynamic permeability in δ direction ($\delta = x, y, z$) can be computed using a combination of weighted and harmonic averaging for parallel layers as follows:

$$k_{\delta_t} = \frac{\sum_{i=1}^{n}\left[A_i\left(\frac{\sum_{j=1}^{m} l_j}{\sum_{j=1}^{m}\frac{l_i}{k_{\delta_j}}}\right)\right]}{\sum_{i=1}^{n} A_i}. \quad (52)$$

In equation (52), A_i and l_j refer to the media (fracture or matrix) area and length, respectively. Additionally, *n* represents the number of media in a plane normal to the flow direction (for k_{z_t} case the plane would be yz plane) and m represents the number of planes (fracture and matrix) that the flow intersects in any direction. For instance, in the z direction n contains (X+Y) number of fractures and (X-1)(Y-1) number of matrix blocks. Extending equation (52), the cube's total dynamic absolute permeability in x, y and z directions is defined as follows:

$$k_{z_t} = \frac{\left(\frac{k_{ft}k_{mt}(L-X(J_o+\Delta J))(L-Y(J_o+\Delta J))}{k_{ft}(L-Z(J_o+\Delta J))+k_{mt}Z(J_o+\Delta J)}\right)+(X+Y)k_{ft}(J_o+\Delta J)}{L}; \quad (53)$$

$$k_{y_t} = \frac{\left(\frac{k_{ft}k_{mt}(L-X(J_o+\Delta J))(L-Z(J_o+\Delta J))}{k_{ft}(L-Y(J_o+\Delta J))+k_{mt}Y(J_o+\Delta J)}\right)+(X+Z)k_{ft}(J_o+\Delta J)}{L}; \text{ and} \quad (54)$$

$$k_{x_t} = \frac{\left(\frac{k_{ft}k_{mt}(L-Z(J_o+\Delta J))(L-Y(J_o+\Delta J))}{k_{ft}(L-X(J_o+\Delta J))+k_{mt}X(J_o+\Delta J)}\right)+(Z+Y)k_{ft}(J_o+\Delta J)}{L}. \quad (55)$$

k_{mt} and k_{ft}in equations (53) to (55) refer to the dynamic absolute permeability of the matrix and fracture, respectively. The dynamic absolute permeability of the matrix, k_{mt}, and the dynamic absolute permeability of the fracture, k_{ft}, are defined by equations (38) and (48), respectively. The averaged dynamic absolute permeability computed from equations (53) to (55) is assigned to the whole block of rock and inserted as a stress-dependent parameter into the solution of capillary imbibition in equation (27).

3.4.3 Total Geo-Dynamic Capillary Pressure ($P_c(t)$)

Capillary pressure refers to the pressure difference which exists at the interface of two immiscible fluids [*Ahmed and McKinney*, 2011]. In general, the capillary pressure curve versus saturation for a porous medium is a function of the (1) pore size, (2) pore size

distribution, (3) pore structure, (4) fluid saturation, (5) fluid saturation history, (6) wettability of the rock and (7) interfacial tension of the fluids involved [*Peters*, 2012].

Capillary pressure is the most effective flow-dynamic and geo-dynamic parameter in this research for capillary-driven spontaneous imbibition. We describe it as *flow-dynamic* because it changes with saturation and *geo-dynamic* because it is a function of stress-dependent pore size. However, it is often necessary to convert the capillary pressure data for cores in the lab to the reservoir condition. This conversion can be done using the Leverett J-function, which is a dimensionless capillary pressure function [*Leverett*, 1941].

$$J(S_w, \Gamma) = \frac{P_c}{\sigma cos\theta}\sqrt{\frac{k}{\varphi}}. \quad (56)$$

Equation (56) suggests that at the same saturation, rocks with the same fabric, Γ, but different static properties (e.g. porosity and permeability) will have a similar Leverett J-function. In this study, we assume that rock fabric does not change with stress, but that voids (porosity) will vary with stress. this allows the Leverett J-function to be used for cases before and after applying effective stress:

$$\frac{P_c(t)}{\sigma cos\theta}\sqrt{\frac{k_t}{\varphi_t}} = \frac{P_c}{\sigma cos\theta}\sqrt{\frac{k_i}{\varphi_i}}, \text{ or} \quad (57)$$

$$P_c(t) = P_c\sqrt{\frac{k_i}{k_t}}\sqrt{\frac{\varphi_t}{\varphi_i}}. \quad (58)$$

Consequently, having previously determined the dynamic total porosity (equation 51) and permeability (equations 53 to 55), equation (58) yields the geo-dynamic capillary pressure for the whole block in the solution for capillary diffusion given in equation (27).

4.4.4 Total Geo-Dynamic Relative Permeability (k_{rt})

Relative permeability curves are flow-dynamic properties of rock and fluid. As summarized previously, several researchers provide different correlations to model the so-called flow-dynamic relative permeability curves based on wetting phase saturation. However, relative permeability curves are stress-dependent and hence are identified as geo-dynamic parameters as well.

While *Khan* [2009], *Hamoud et al.* [2012] and *Ojagbohunmi et al.* [2012] have presented empirical functions relating porosity change fraction and relative permeability end-points for Canadian oil sands, similar relationships are required for carbonates. As discussed previously, two lab experimental programs on naturally fractured carbonate undertaken by *McDonald et al*. [1991] and *Lian et al*. [2012] provided opposite results in terms of the changes to irreducible water saturation with compaction. Both experimental programs showed that wettability, in addition to pore size, must be considered to explain stress-dependent relative permeability end-points. This suggests that the water-wet rock for the experiment of *McDonald et al.* [1991] does not behave in the same manner as the mix-wet rock used in the *Lian et al.* [2012] experiment. Given the more common condition of mixed wettability for NFCRs, the results from *Lian et al.* [2012] are used in this study.

Since capillary pressure allows us to capture the pore size and wettability effect, as well as to identify phase trapping and the end-points of relative permeability, we have modified the form of the empirical functions developed by *Khan* [2009], *Hamoud et al.* [2012] and *Ojagbohunmi et al.* [2012] to derive the following equations to describe the

relationship between the end-points of geo-dynamic relative permeability and geo-dynamic capillary pressure:

$$S_{wir}(t) = S_{wir}\left(-12.15 + 13.15\left(\frac{P_c(t)}{P_c}\right)\right); \quad (59)$$

$$S_{nwr}(t) = S_{nwr}\left(-2.75 + 3.75\left(\frac{P_c(t)}{P_c}\right)\right); \quad (60)$$

$$K_{rw-max}(t) = K_{rw-max}\left(38.52 - 37.52\left(\frac{P_c}{P_c(t)}\right)\right); \text{ and} \quad (61)$$

$$K_{rnw-max}(t) = K_{rnw-max}\left(1.001 - 0.001\left(\frac{P_c}{P_c(t)}\right)\right). \quad (62)$$

All of the constants in equations (59) to (62) have been estimated using the least square technique, based on the data on stress-dependent relative permeability at 10 MPa and 30 MPa effective stress reported in *Lian et al.*'s [2012] experiment. For validation, we compute the relative permeability curves for the case of effective confining stress of 20 MPa and then compare it with experimental data (circle symbols in Figure 8). As illustrated in Figure 8, equations (59) to (62) provide an excellent match with the experimental results for 20 MPa effective confining stress.

All of the equations required for the stress-dependent counter-current spontaneous imbibition semi-analytical method have now been described. Figure 9 provides a flow chart summarizing the analysis workflow, which has been coded in Matlab.

4 Results

In this section, we utilize the semi-analytical model to investigate the geomechanical impacts on spontaneous imbibition and oil recovery in a cubic block of fractured carbonate rock with three orthogonal fractures parallel with the block sides. Capillary pressure table for the case of mixed-wet fractured carbonate [*Lian et al.*, 2012] is used as input in the model. Additional rock and fluid properties based on a real carbonate reservoir case are summarized in Table 4 [*Haghi et al.* 2018; *Haghi et al.* 2013]. In the simulations, the effective confining stress is considered an input variable at the beginning of the procedure (Figure 9). The stress-dependent porosity, absolute permeability, capillary pressure and end-points of the relative permeability curve are calculated based on equations (51), (52), (58) and (59) to (62), respectively, and illustrated in Figure 10. As Figure 10a) clearly shows, the difference between the capillary pressure curves in the effective confining stress range of 20 MPa to 30 MPa is much less than the difference in the range between 10 MPa and 20 MPa. This is due to the effect of non-linear fracture closure at high stresses.

We use modified *Brooks and Corey* [1966] type curves to numerically fit the experimental capillary pressure data and define the curvature of geo-dynamic capillary pressure curves (equation 1). The process of finding the pore size distribution index ($\lambda = -1/\beta$) requires the creation of a log-log plot of S_w^* (equation 4) versus P_c , as shown in the workflow in Figure 9. Based on the *Brooks-Corey* [1966] model, i.e. equation (63), the graph must be linear. If the graph is nonlinear, λ is adjusted iteratively until the graph becomes linear (Figure 11).

$$lnS_w^* = -\lambda lnP_c + \lambda lnP_e \quad (63)$$

The fitting constants in equations (6) and (7) are estimated next using the least square method as $A = -1.5$, $A' = -8.5$, $B = 2.955$, and $B' = 12.045$. Using the semi-analytical framework described above, all of the stress-dependent properties thus calculated are inserted into equation (27), which allows the geo-dynamic capillary-driven fractional flow (F) to be determined. As mentioned previously, C' in equation (20) is no longer a constant but a stress-dependent parameter. Thus, at each stress state, it should be recalculated iteratively to fit the F function into the limits of 0 to 1 for S_{wir} to ($1-S_{or}$), respectively. Figure 12 compares the geo-dynamic Buckley-Leverett and capillary-drive fractional flow curves. Both methods present distinct curves for 10, 20, and 30 MPa effective confining stress; these shift from left to right from the 10 MPa curve to the 30 MPa curve. As illustrated in Figure 13, for the given carbonate block dimensions and properties in Table 4, increasing the effective stress from 10 MPa to 30 MPa, the model developed in this study predicts that the recovery factor of the block will decrease by approximately 50%. This highlights the significant impact geomechanical processes may have on oil recovery in NFCRs.

Finally, the saturation curve versus similarity variable ω, shown in Figure 14, also illustrates the stress dependency of ω in spontaneous imbibition. As noted in Figure 14, $\omega(S_w = S_{wir})$ increases as the effective confining stress decreases from 30 MPa to 10 MPa. Using equation (25), early time imbibition (t^*) is computed equal to 0.86, 4.64, and 11.69 hours for the cases of 10 MPa, 20 MPa, and 30 MPa effective confining stress, respectively. The reduced imbibition times at lower effective confining stresses are primarily the result of higher transmissibility in the less deformed rock.

5 Discussion

Water-wet NFCRs are among the best examples of spontaneous capillary imbibition in nature [*Peters*, 2012]. Many authors have assumed that fractures have small or negligible capillary pressure [*Peters*, 2012; *Elfeel et al.*, 2016]. At equilibrium condition, the capillary pressures in the fracture and matrix must be equal at their boundary (equation 64).

$$P_{cf} = P_{cm}. \tag{64}$$

When the 100% saturated fractures make contact with the oil saturated matrix blocks, the capillary equilibrium is disturbed. Hence, fluid exchanges between the fracture and matrix block occur to recover the capillary equilibrium condition. Water and oil are exchanged between two media until the water saturation in the matrix is increased to the maximum possible value over time ($S_w = 1 - S_{or}$).

Injection and production operations change the pore pressure within the pore spaces. Based on poroelasticity theory [*Detournay and Cheng*, 1993], effective stress change leads to pore size changes (bigger or smaller depending on the process). It is well known that capillary pressure is a function of the pore size of the porous media. Accordingly, effective stress should directly affect capillary diffusion in the reservoir. Furthermore, some experimental results on NFCRs have proven the stress-dependency of the end-points and wettability of the relative permeability curves. This is again a result of changing the pore size due to stress. Experiments have shown that the irreducible water saturation increased

significantly as confining stress increased in the case of mixed-wet carbonate rock. Accordingly, when applying higher effective stress, the rock tends to be stronger water-wet. However, in cases where higher effective stress was applied to of strong water-wet rock, the irreducible water saturation decreased.

These findings will be developed and further validated in our next publications. Both our consecutive experimental program and our advanced coupled flow-geomechanical approach will be used to apply the concept of geo-dynamic spontaneous imbibition in naturally fractured carbonates within models ranging from the block scale to the reservoir scale.

5.1. Comparison between Stress-Dependent and Independent Spontaneous Imbibition

In the current semi-analytical model of geo-dynamic spontaneous imbibition, the derived equations for porosity, absolute permeability, capillary pressure, and relative permeability are all based on effective stress. Thus, the effective stress is the input of the solution (see the workflow presented in Figure 9). Generally, spontaneous imbibition by itself does not change effective stress; it only controls saturation distribution and fluid exchanges. To obtain a model of effective stress change over time, we need a reservoir model that includes injecting and producing wells in which the pore pressure changes with time. In that case, spontaneous imbibition is not the only production mechanism, as viscous forces, which change pore pressure, are also involved in production. Hence, the semi-analytical workflow given in Figure 9 is part of a larger code that calculates effective stress as a function of time.

This study focuses only on modelling the capillary imbibition from fracture to a block of rock in different stress conditions. However, to compare the spontaneous imbibition oil recovery predicted by a semi-analytical geo-dynamic solution (scenario 1, given in section 3) with that predicted by a stress-independent solution (scenario 2), we assume that, uniformly over a 50-hour period, the whole block (matrix and fracture) undergoes polynomial build-up in effective stress from 10 MPa to 30MPa in scenario 1 and no effective stress control in scenario 2 (see horizontal projection in Figure 17). The scenario 1 solution given in section 3 can easily be converted to that of scenario 2 by positing that A=0 in equation (27) and implementing stress-independent porosity, absolute permeability, capillary pressure, and relative permeability curves. Figure 15 compares changes in porosity and absolute permeability of the block over time between scenario 1 and scenario 2. Additionally, Figure 16 illustrates the geo-dynamic relative permeability and capillary pressure curves for the block in which the colors indicate time lapse.

Note that in this analysis, both cases start from the same initial condition. However, as Figure 17 reveals, their oil recovery lines increase in different ways. In Figure 17, the colors indicate the effective stress value; comparing the oil recovery from both scenarios (illustrated in the vertical projection), it is evident that the negligible difference present at early times turns into a significant drop in spontaneous imbibition oil recovery at later times. This is due to the impact of rock and fracture deformation in response to increase in effective stress. In the case of scenario 1, the oil recovery initially increases sharply, but by the time, its rate of increase attenuates. Additionally, Figure 17 illustrates the 3D nature of oil recovery curve in reservoir management.

6 Conclusions

The current study presents comprehensive insights into stress-dependent spontaneous imbibition in NFCRs by defining capillary-drive fractional flow and geo-dynamic rock properties. We presented a semi-analytical solution for geo-dynamic capillary-driven fractional flow equation in NFCRs. To do so, we derived analytical equations to specify the unknown stress-dependent parameters in our semi-analytical solution. We characterized the geo-dynamic behavior of intact rock and fracture independently based on poroelastic and nonlinear fracture stiffness equations and combined them with equivalent continuum concepts. The results from the semi-analytical solution for the case of mixed-wet NFCRs reveals a 50 percent reduction in the oil recovery factor as effective confining stress increases from 10 MPa up to 30 MPa. This proves the significant impact of effective stress on spontaneous imbibition in NFCRs.

Appendix A: Derivation of Similarity Variable

As noted in section 3.1, the one boundary condition for the unidirectional displacement of the non-wetting phase by entry of the wetting phase during spontaneous imbibition (ignoring the gravity) is:

$$q_w(x=0,t)=\frac{C}{\sqrt{t}}. \tag{A1}$$

Now, recalling the continuity equation (Equation 10), at x=0 we have:

$$\frac{\partial}{\partial t}(S_w\varphi)=-\frac{\partial}{\partial x}\left(F\frac{C}{\sqrt{t}}\right). \tag{A2}$$

where the capillary-driven fractional flow function F is defined as [*McWhorter and Sunada*, 1990]:

$$F=\frac{q_w}{q_w(x=0,t)}. \tag{A3}$$

As the term $\frac{C}{\sqrt{t}}$ in equation (A2) is independent from x, equation (A2) can be rewritten as follows:

$$-\frac{\partial}{\partial t}(S_w\varphi)=\frac{C}{\sqrt{t}}\frac{\partial F}{\partial x}. \tag{A4}$$

Similarly, it may be written as

$$\frac{C}{\sqrt{t}}\frac{\partial F}{\partial S_w}\frac{\partial S_w}{\partial x}+\frac{\partial(S_w\varphi)}{\partial t}=0. \tag{A5}$$

Equation (A5) is a hyperbolic PDE. Based on calculus, the total differential of $S_w\emptyset$ is given by

$$\frac{\partial(S_w\varphi)}{\partial x}\frac{dx}{dt}+\frac{\partial(S_w\varphi)}{\partial t}=\frac{d(S_w\varphi)}{dt}. \tag{A6}$$

Subtracting equation (A5) from equation (A6), we obtain

$$\left(\varphi\frac{dx}{dt}-\frac{C}{\sqrt{t}}\frac{\partial F}{\partial S_w}\right)\frac{\partial S_w}{\partial x}=\frac{d(S_w\varphi)}{dt}. \tag{A7}$$

In equation (A7), the porosity (ϕ) is considered to be independent from *x*. One can decompose equation (A7) into the following simultaneous equations:

$$\left(\varphi\frac{dx}{dt}-\frac{C}{\sqrt{t}}\frac{\partial F}{\partial S_w}\right)=0 \tag{A8}$$

$$\frac{d(S_w\varphi)}{dt} = 0. \tag{A9}$$

Equation (A9) indicates a fixed $S_w\varphi$ along the characteristic path given in equation (A8). Integrating equation (A8) to measure the distance *x* traveled by constant $S_w\varphi$ at a time *t*, we arrived at to the following relation for the similarity variable:

$$\frac{2C}{\varphi}\frac{\partial F}{\partial S_w} = \frac{x}{\sqrt{t}} = \omega \tag{A10}$$

Acknowledgements

The authors wish to thank the Computer Modelling Group (CMG) for providing access to their software. The financial support of the Foundation CMG Industrial Research Consortia on Reservoir Geomechanics is highly appreciated. We also thank the anonymous reviewers for their valuable comments.

Additionally, readers can access the data used in the current semi-analytical (theoretical) study in published paper by *McDonald et al.* [1991], *Lian et al.* [2012], *Haghi et al.* [2018], *Schmid et al.* [2016], and *Haghi et al.* [2013].

References

Ahmed, T., & McKinney, P. (2011). *Advanced reservoir engineering.* Gulf Professional Publishing.

Bagheri, M., & Settari, A. (2008). *Modeling Fluid Flow in Deformable Fractured Reservoirs using Full Tensor permeability*. Paper SPE 113319 presented at the 2009 SPE Europec. In EAGE Annual Conference and Exhibition, Rome, Italy (pp. 9-12).

Bandis, S. C., Lumsden, A. C., & Barton, N. R. (1983). Fundamentals of rock joint deformation. *International Journal of Rock Mechanics and Mining Sciences & Geomechanics Abstracts*, Vol. 20, No. 6, pp. 249-268. https://doi.org/10.1016/0148-9062(83)90595-8

Barton, N., Bandis, S., & Bakhtar, K. (1985). Strength, deformation and conductivity coupling of rock joints. *International Journal of Rock Mechanics and Mining Sciences & Geomechanics Abstracts*, Vol. 22, No. 3, pp. 121-140. https://doi.org/10.1016/0148-9062(85)93227-9

Bear, J. (2013). Dynamics of fluids in porous media. Courier Corporation.

Behbahani, H., & Blunt, M. J. (2005). Analysis of Imbibition in Mixed-Wet Rocks Using Pore-Scale Modeling. *SPE Journal* 10 (4): 466–474. SPE-90132-PA. https://doi.org/10.2118/90132-PA

Brooks, R. H., & Corey, A. T. (1966). Properties of porous media affecting fluid flow. *Journal of the Irrigation and Drainage Division*, 92(2), 61-90.

Carman, P.C., (1956). *Flow of gases through porous media*. Academic press.

Corey, A. T. (1954). The interrelation between gas and oil relative permeabilities. *Producers monthly*,19(1), 38-41.

Cundall, P. A., & Lemos, J. V. (1990). *Numerical simulation of fault instabilities with a continuously-yielding joint mode*l. Rockbursts and Seismicity in Mines, Balkema, S, 147-52

Dake, L. P. (1983). *Fundamentals of reservoir engineering* (Vol. 8). Elsevier.

Detournay, E., & Cheng, A. H. D. (1993). Fundamentals of poroelasticity, Comprehensive Rock Engineering, Vol 2: *Analysis and Design Methods*, Eds. Brown, ET, Fairhurst, CH and Hoek, E.

Elfeel, M. A., Al-Dhahli, A., Geiger, S., & van Dijke, M. I. (2016). Fracture-matrix interactions during immiscible three-phase flow. *Journal of Petroleum Science and Engineering*, 143, 171-186. https://doi.org/10.1016/j.petrol.2016.02.012

Ferno, M. A. (2012). *Enhanced Oil Recovery in Fractured Reservoirs, Introduction to Enhanced Oil Recovery (EOR) Processes and Bioremediation of Oil-Contaminated Sites*. ISBN, 978-953.

Haghi, A. H., Kharrat, R., Asef, M. R., & Rezazadegan, H. (2013). Present-day stress of the central Persian Gulf: implications for drilling and well performance. *Tectonophysics*, 608, 1429-1441. https://doi.org/10.1016/j.tecto.2013.06.001

Haghi, A. H., Chalaturnyk, R., & Ghobadi, H. (2018). The state of stress in SW Iran and implications for hydraulic fracturing of a naturally fractured carbonate reservoir. *International Journal of Rock Mechanics and Mining Sciences*, 105, 28-43. https://doi.org/10.1016/j.ijrmms.2018.03.002

Hamoud, M., R.J. Chalaturnyk and J. Leung. 2012. *Influence of Geomechanical Processes on Relative Permeability*. Canadian Rock Mechanics Symposium, Edmonton, Alberta, 9 p.

Hudson, J. A., & Harrison, J. P. (2000). *Engineering rock mechanics-an introduction to the principles*. Elsevier.

Huo, D., & Benson, S. M. (2016). Experimental investigation of stress-dependency of relative permeability in rock fractures. *Transport in Porous Media*, 113(3), 567-590. **https://doi.org/10.1007/s11242-016-0713-z**

Khan, A. H. 2009. *Shear Induced Relative Permeability Changes in Uncemented Sands.* Masters of Science in Engineering Thesis, December 2009, University of Texas at Austin, USA.

Leverett, M. (1941). Capillary behavior in porous solids. *Transactions of the AIME*, 142(01), 152-169. https://doi.org/10.2118/941152-G

Li, P., Chalaturnyk, R. J., & Tan, T. B. (2003). *Coupled reservoir geomechanical simulations for the SAGD process*. In Canadian international petroleum conference. Petroleum Society of Canada.

Li, K., & Horne, R. N. (2006). Comparison of methods to calculate relative permeability from capillary pressure in consolidated water-wet porous media. *Water resources research*, 42(6). https://doi.org/10.1029/2005WR004482

Lian, P., & Cheng, L. (2012). The characteristics of relative permeability curves in naturally fractured carbonate reservoirs. *Journal of Canadian Petroleum Technology*, 51(02), 137-142. https://doi.org/10.2118/154814-PA

McDonald, A. E., Beckner, B. L., Chan, H. M., Jones, T. A., & Wooten, S. O. (1991). *Some important considerations in the simulation of naturally fractured reservoirs. In Low Permeability Reservoirs Symposium*. Society of Petroleum Engineers.

McWhorter, D. B., & Sunada, D. K. (1990). Exact integral solutions for two-phase flow. *Water Resources Research*, 26(3), 399-413. https://doi.org/10.1029/WR026i003p00399

Nelson, R.A. (2001). *Geologic Analysis of Naturally Fractured Reservoirs*. Gulf Publishing.

Ojagbohunmi, S., Chalaturnyk, R. J., & Leung, J. Y. W. (2012, January). *Coupling of Stress-Dependent Relative Permeability and Reservoir Simulation*. In SPE Improved Oil Recovery Symposium. Society of Petroleum Engineers.

Pariseau, W. G. (2011) *Design Analysis in Rock Mechanics 2nd Edition*, CRC Press, Appendix B

Peters, E. J. (2012). *Advanced Petrophysics: Dispersion, interfacial phenomena (Vol. 2).* Greenleaf Book Group.

Pooladi-Darvish, M., & Firoozabadi, A. (2000). Cocurrent and countercurrent imbibition in a water-wet matrix block. *SPE Journal*, 5(01), 3-11. https://doi.org/10.2118/38443-PA

Schmid, K. S., Alyafei, N., Geiger, S., & Blunt, M. J. (2016). Analytical solutions for spontaneous imbibition: fractional-flow theory and experimental analysis. *SPE Journal*, 21(06), 2-308. https://doi.org/10.2118/184393-PA

Schmid, K. S., & Geiger, S. (2012). Universal scaling of spontaneous imbibition for water-wet systems. *Water resources research*, 48(3). https://doi.org/10.1029/2011WR011566

Segall, P. (1989). Earthquakes triggered by fluid extraction. *Geology*, 17(10), 942-946. https://doi.org/10.1130/0091-7613(1989)017<0942:ETBFE>2.3.CO;2

Settari, A., Walters, D. A., & Behie, G. A. (1999). *Reservoir geomechanics: New approach to reservoir engineering analysis.* In Technical Meeting/Petroleum Conference of The South Saskatchewan Section. Petroleum Society of Canada.

Tortike, W. S., & Ali, S. M. (1993). Reservoir simulation integrated with geomechanics. *Journal of Canadian Petroleum Technology*, 32(05). https://doi.org/10.2118/93-05-02

Wang, H. F. (2017). *Theory of linear poroelasticity with applications to geomechanics and hydrogeology*. Princeton University Press.

Wang, H. (2000). *Theory of linear poroelasticity with applications to geomechanics and hydrogeology*. Princeton University Press.

Warren, J. E., & Root, P. J. (1963). The behavior of naturally fractured reservoirs. *SPE Journal*, 3(03), 245-255. https://doi.org/10.2118/426-PA

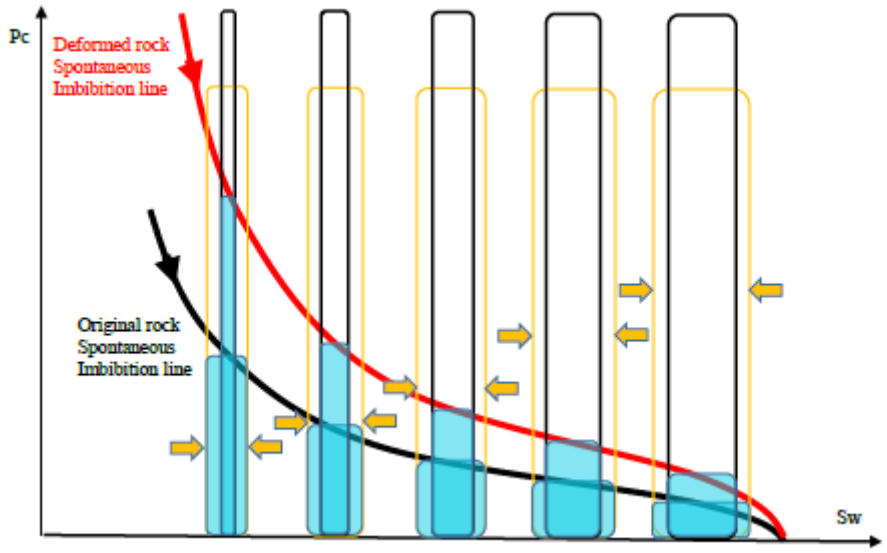

Figure 1. Schematic Description of Stress-dependent Spontaneous Imbibition Curve in a Bundle of Capillary Tubes

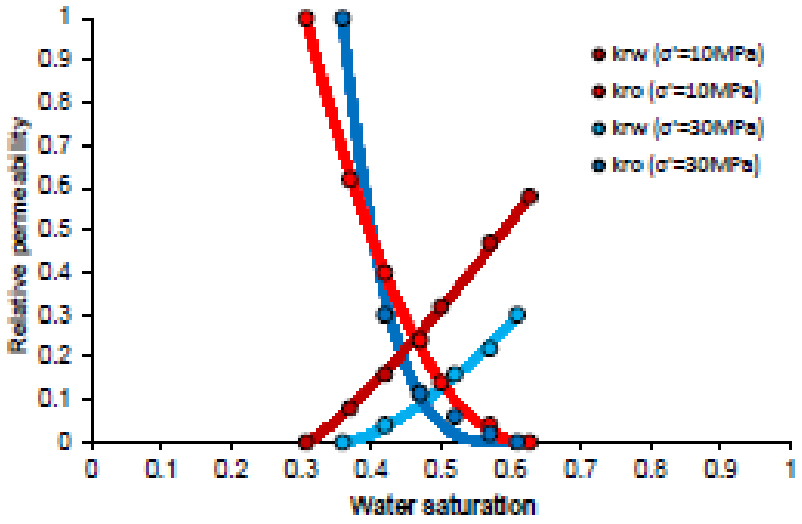

Figure 2. Relative Permeability Curves Based on Lian et al.'s [2012] Experiment. The dots define the experimental data and the solid lines indicate the curve fitting lines.

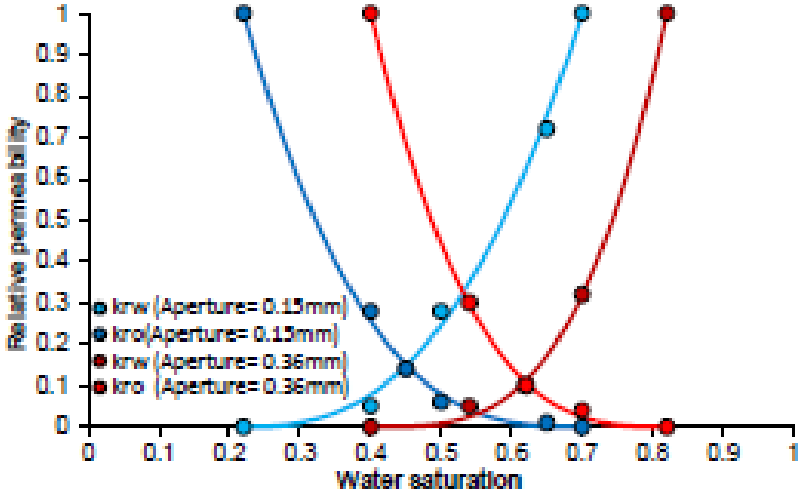

Figure 3. Relative Permeability Curves Based on McDonald et al.'s [1991] Experiment. The dots define the experimental data and the solid lines indicate the curve fitting lines.

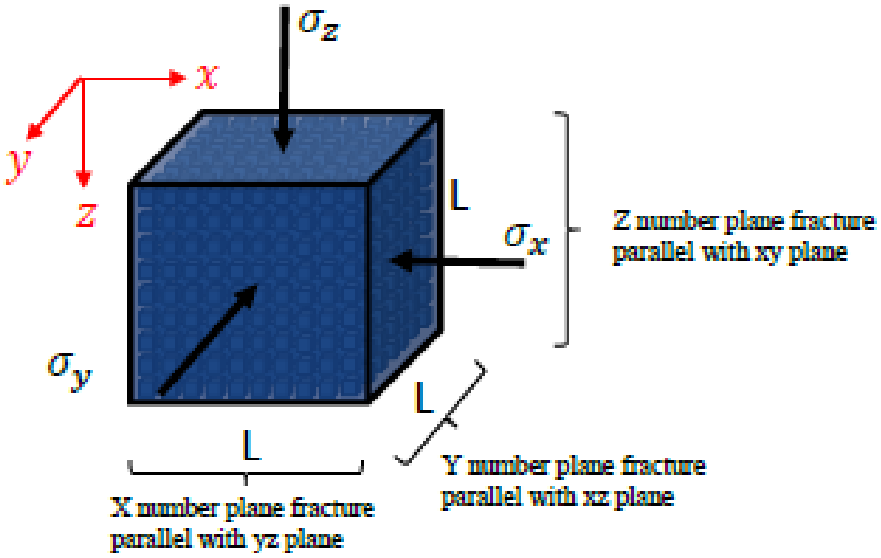

Figure 4. Block Model Consisting of X*Y*Z of Orthogonal Plane Fractures

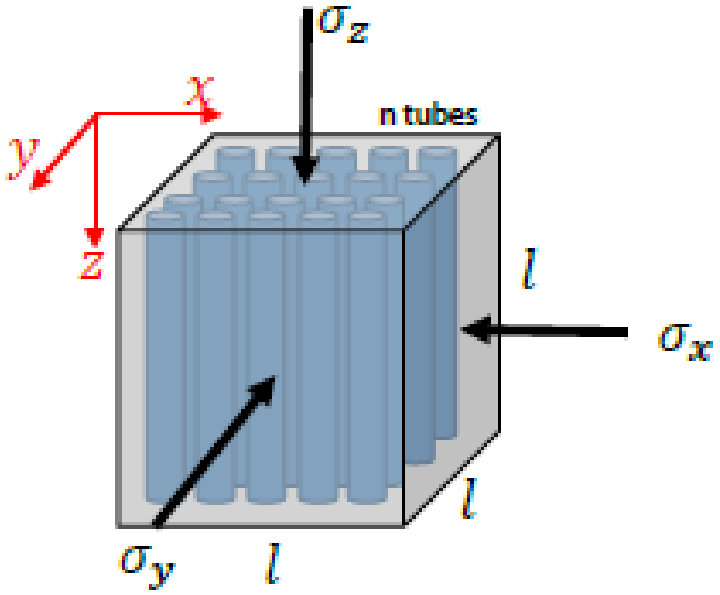

Figure 5. Deformation of Matrix Block Due to Effective Confining Stress

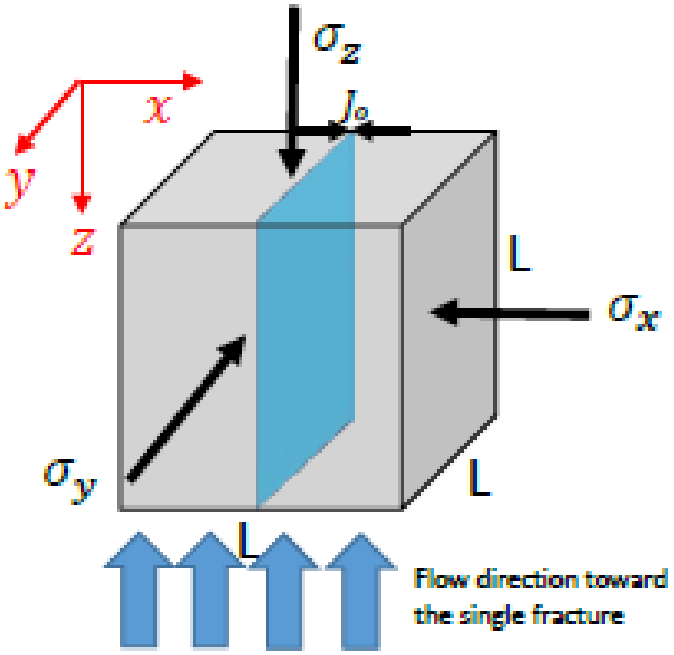

Figure 6. Arbitrary Fracture Geometry Inside the Block Model

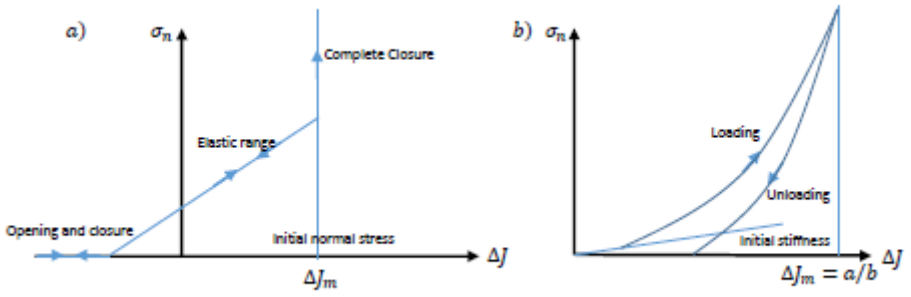

Figure 7. Fracture Closure versus Normal Stress in a) Linear and b) Nonlinear Methods

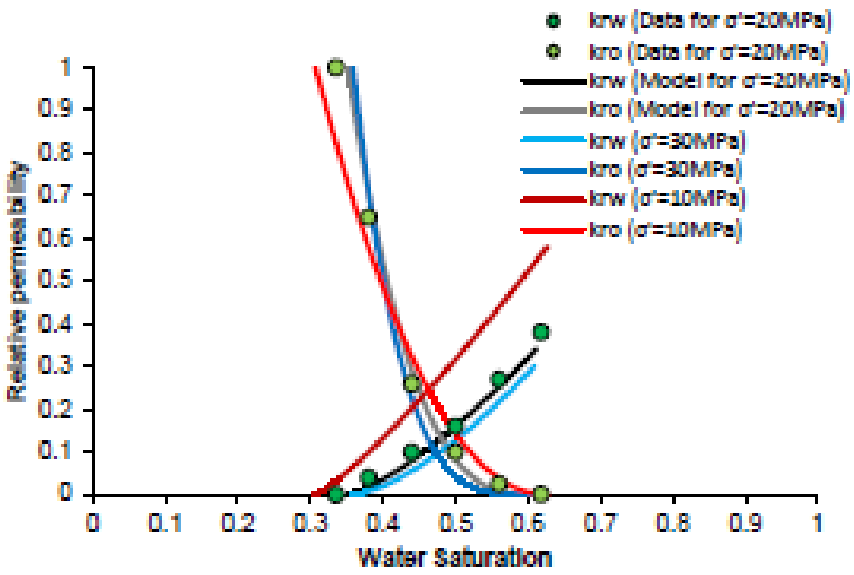

Figure 8. Investigation of the Accuracy of Equations (59) to (62) for Relative Permeability Curves in the Case of 20 MPa Effective Confining Stress

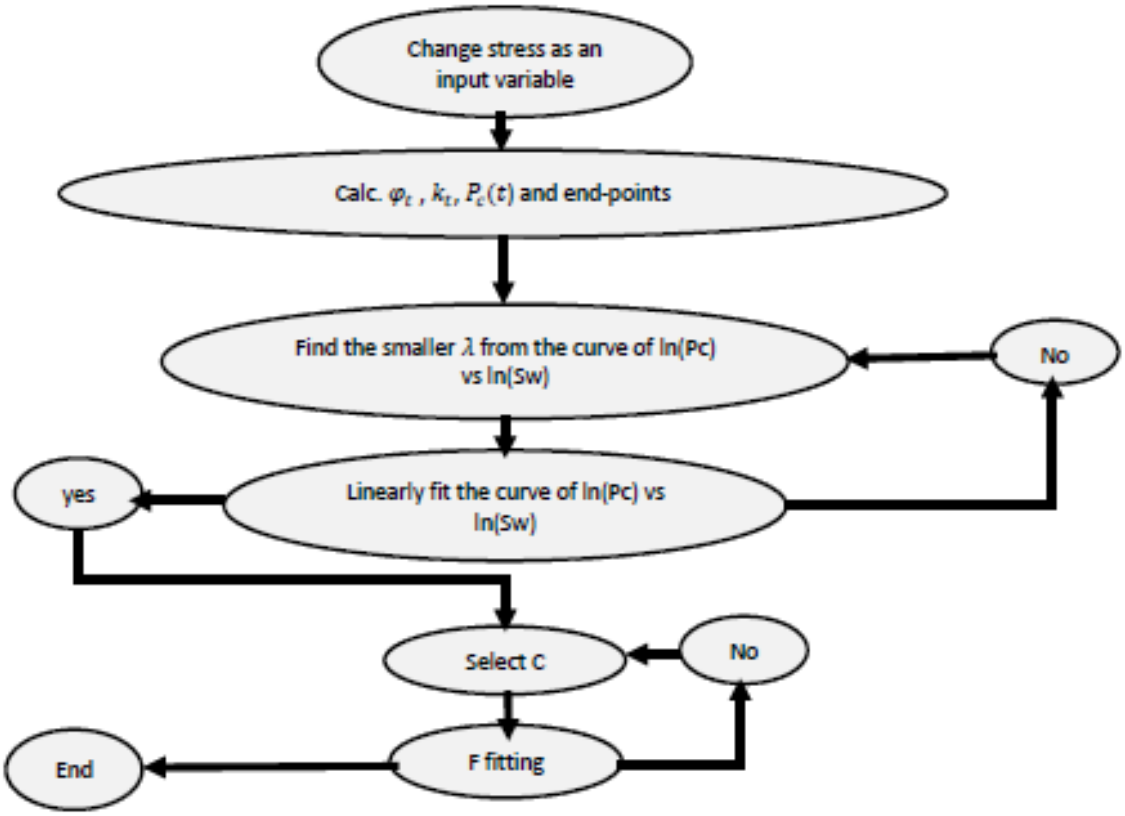

Figure 9. Work Flow of the Semi-analytical Solution for Stress-dependent Capillary Imbibition

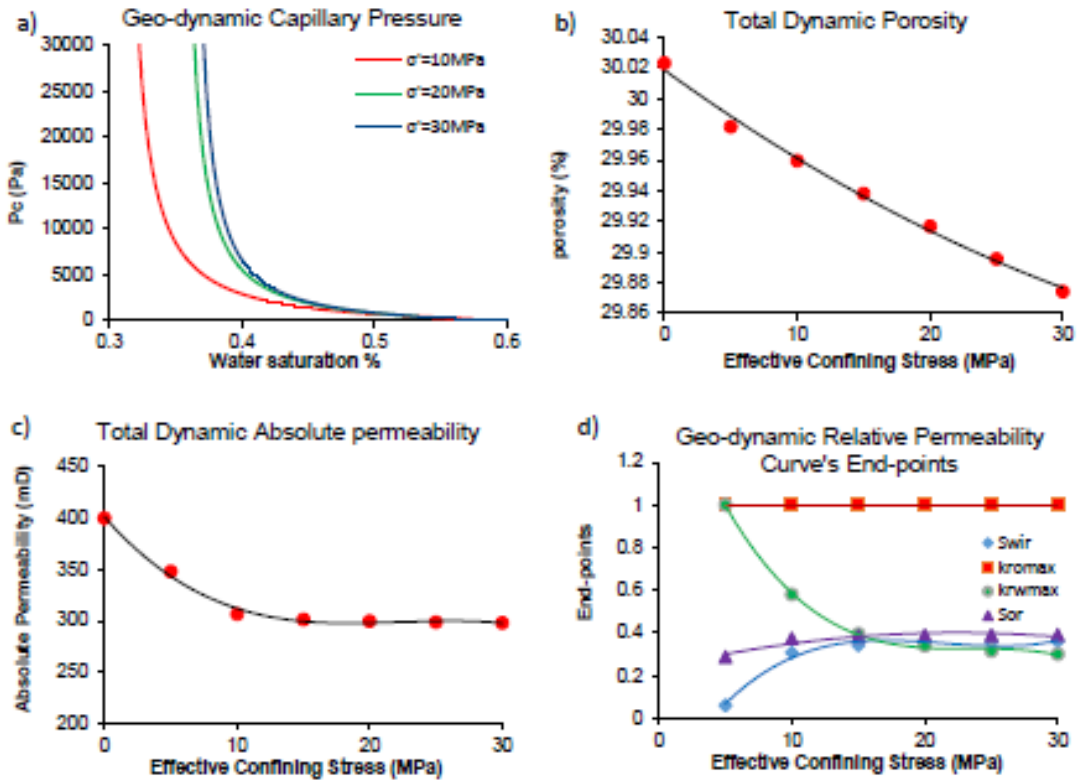

Figure 10. Variation in Stress-dependent Spontaneous Imbibition Parameters a) $P_c(t)$,b) φ_t c) k_t, and d) k_{rt} End-points

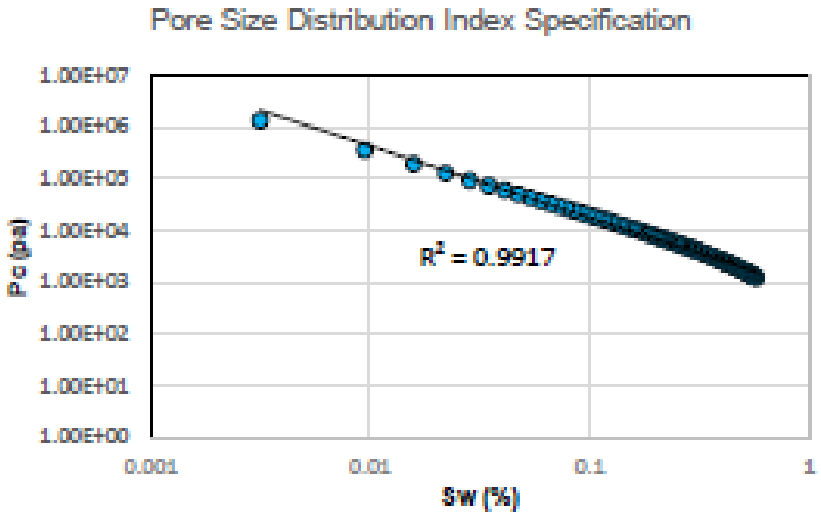

Figure 11. Capillary Pressure versus Wetting Phase Saturation and the Fitted Line Representing the Linearity of Data in a Log-Log Scale

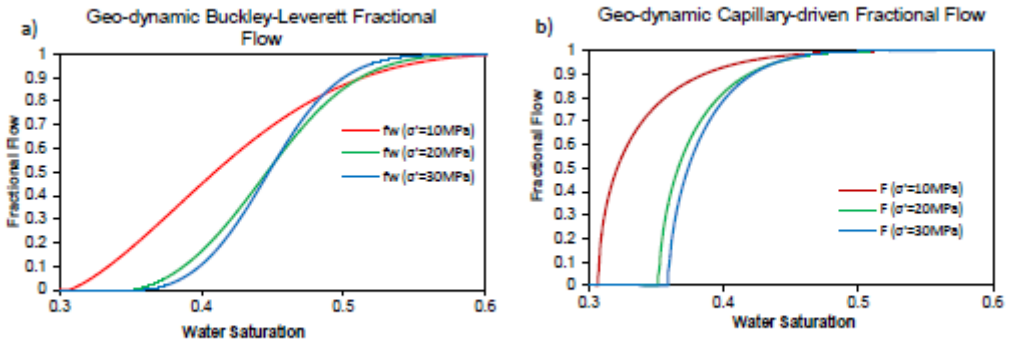

Figure 12. Comparison between the a) Geo-dynamic Buckley-Leveret and b) Capillary Driven Fractional Flow in NFCRs

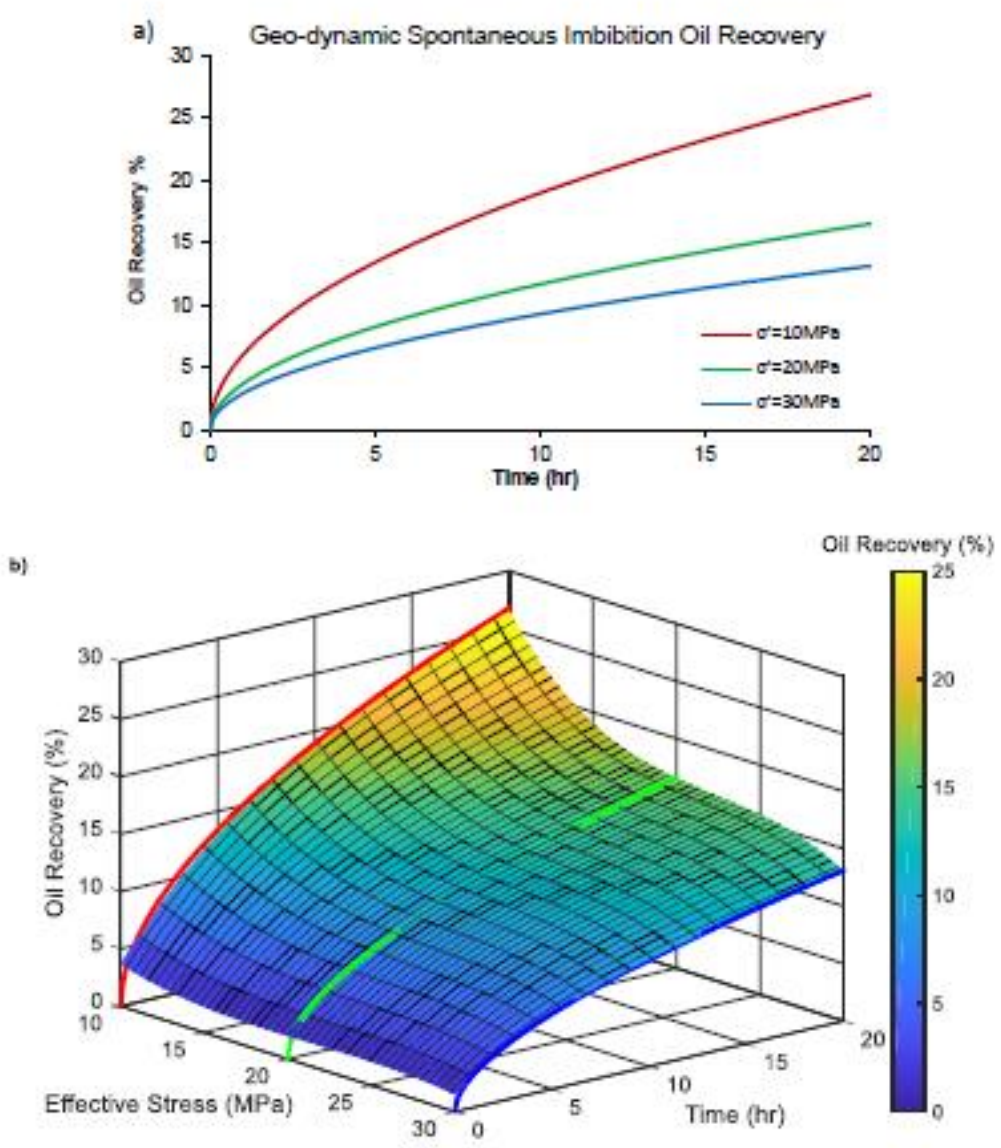

Figure 13. Oil Recovery Profile for NFCRs as a Function of Changes to Effective Confining Stress in 2D and 3D Scales

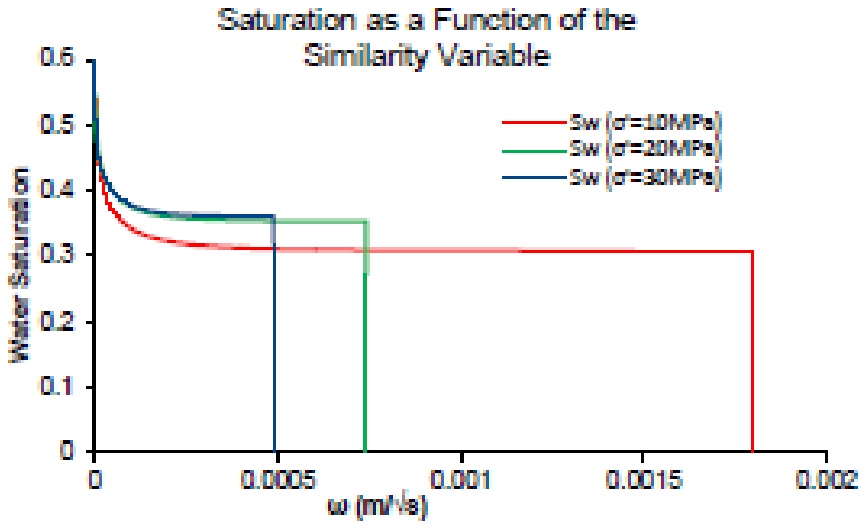

Figure 14. Saturation Profiles for 10, 20 and 30 MPa Effective Confining Stress

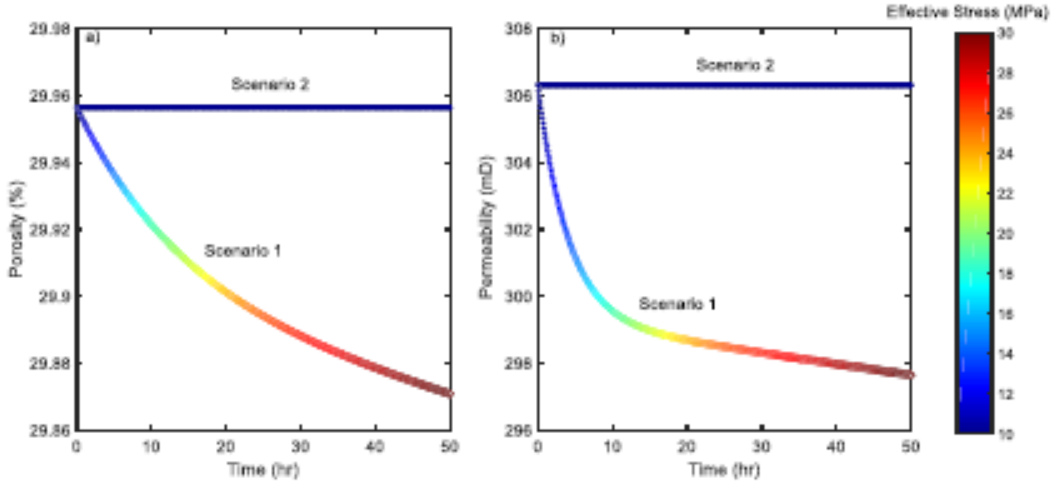

Figure 15. Comparison of a) Porosity and b) Permeability Changes with time and stress to a Block of Rock. Scenario 1: Geo-dynamic Spontaneous Imbibition. Scenario 2: Stress-independent Spontaneous Imbibition.

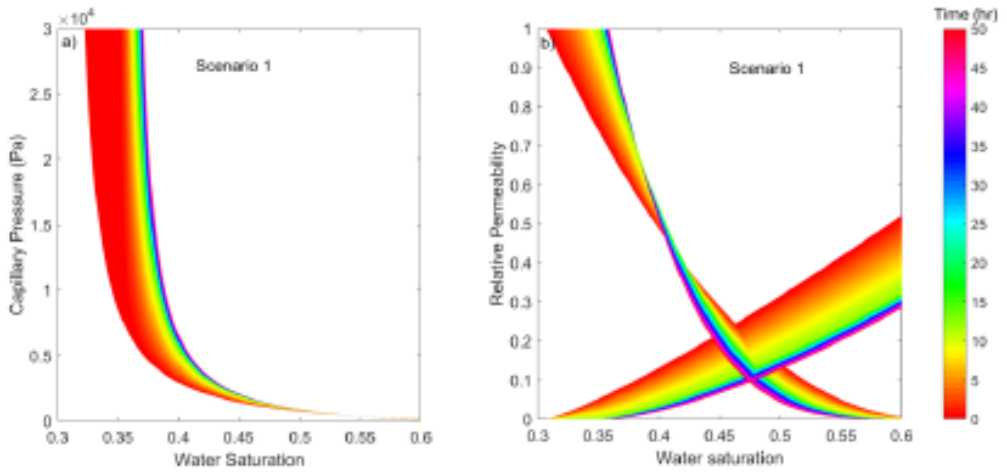

Figure 16. Changes in a) Relative Permeability and b) Capillary Pressure Curves over Time in Scenario 1 (Geo-dynamic Spontaneous Imbibition)

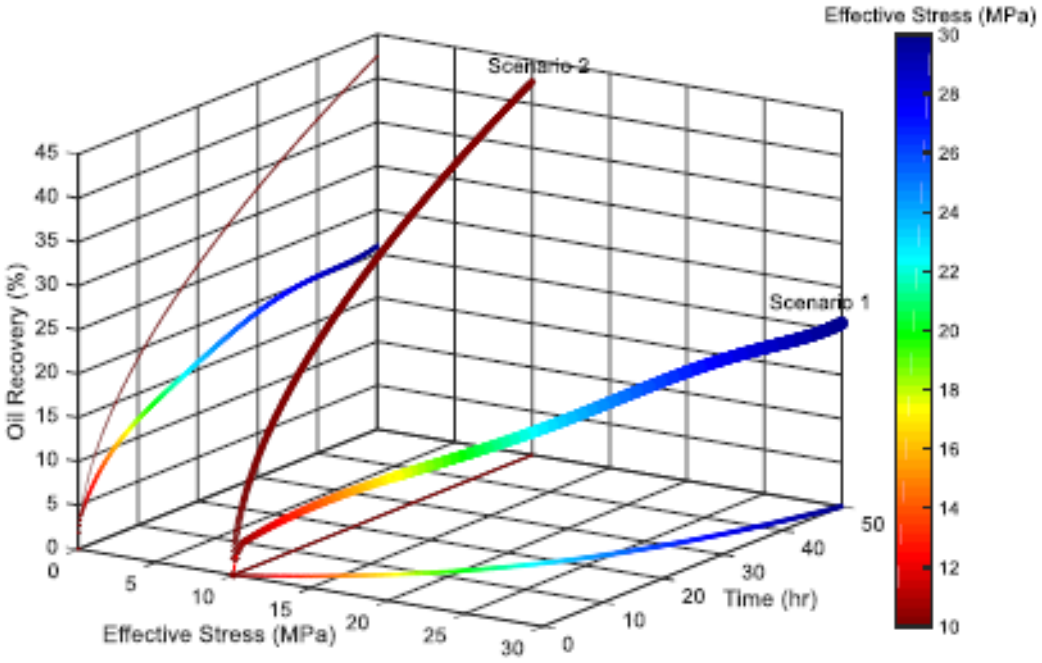

Figure 17. Comparison of Oil Recovery from a Block of Rock Between Geo-dynamic Spontaneous Imbibition (Scenario 1) and Stress-Independent Spontaneous Imbibition (Scenario 2)

Table 1. Modified Brooks and Corey Equation to fit Curves on the Lian et al.'s [2012] Experimental Data

Relative Permeability	$\boldsymbol{\sigma' = 10MPa}$	$\boldsymbol{\sigma' = 30MPa}$
k_{rw}	$0.58 \times \left(\frac{S_w - 0.307}{0.32}\right)^{1.2}$	$0.3 \times \left(\frac{S_w - 0.359}{0.25}\right)^{1.5}$
k_{rnw}	$1 \times \left(\frac{0.627 - S_w}{0.32}\right)^{2.1}$	$1 \times \left(\frac{0.609 - S_w}{0.25}\right)^{3.8}$

Table 2. Modified Brooks and Corey Equations to fit curves on the McDonald et al.'s [1991] Experiment Data

Relative Permeability	**Aperture = 0.36 mm ($\sigma' = 6.9MPa$)**	**Aperture = 0.15 mm ($\sigma' = 26.5MPa$)**
k_{rw}	$1 \times \left(\frac{S_w - 0.4}{0.42}\right)^{3.4}$	$1 \times \left(\frac{S_w - 0.22}{0.48}\right)^{2.6}$
k_{rnw}	$1 \times \left(\frac{0.82 - S_w}{0.42}\right)^{3}$	$1 \times \left(\frac{0.7 - S_w}{0.48}\right)^{2.9}$

Table 3. Initial and Boundary Conditions for the Semi-analytical Model Shown in Figure 4

Initial Conditions	**Boundary Conditions**
$\varphi(x,0) = \varphi_0$	$S_w(L/2,t) = 1 - S_{or}$
$S_w(x,0) = S_{wir}$	$q_w(0,t) = Ct^{1/2}$

Table 4. Parameter Set for Semi-analytical Model

Parameter	Units	Value	Parameter	Units	Value
L	m	0.1	k_{fi}	m^2	9.1E-11
k_{mi}	m^2	3.0E-16	ϑ	-	0.3
φ_{mi}	-	0.3	E	MPa	20000
k_{nn}	MPa/m	20014	α	-	0.7
V_o	m	0.000033	μ_w	$Pa.s$	0.001
φ_{fi}	-	0.00033	μ_o	$Pa.s$	0.003